Progress in Engineering Science 3 (2026) 100285

Contents lists available at ScienceDirect

Progress in Engineering Science

journal homepage: www.sciencedirect.com/journal/progress-in-engineering-science

Investigating thermal performance of 3D-printed cubic lattices integrated in bio-based nonwoven assemblies under wind exposure

Mostafa Alakhdar [a,b,*], Ludwig Vinches [b,c], Stéphane Hallé [a]

[a] Dept. of Mechanical Engineering, École de Technologie Supérieure, 1100 Notre-Dame West, Montréal, Quebec, Canada
[b] Centre de Recherche en Santé Publique (CReSP), Montréal, Quebec, Canada
[c] Dept. of Environmental and Occupational Health, Université de Montréal, 2375 chemin de la Côte-Sainte-Catherine, Montreal, Quebec, Canada

ARTICLE INFO

Keywords:
Thermal resistance
Nonwoven
3D-printed lattice
Textile assembly
Wind exposure

ABSTRACT

Cold-weather protective clothing must retain high thermal resistance in windy environments. 3D-printed lattice structures present a novel approach to enhancing the thermal resistance of textile assemblies; however, their potential for wind protection and airflow management remains largely unexplored. This study experimentally investigates the heat transfer behavior of a hybrid insulating composite consisting of a bio-based nonwoven textile integrated with a 3D-printed cubic lattice structure. Five lattice opening ratios (0 –100%) were integrated with the nonwoven in two configurations with the lattice positioned either above the nonwoven or beneath it. These configurations were evaluated to quantify how geometric arrangement influences airflow and thermal resistance. Standardized ISO 11092 tests were performed under controlled horizontal wind (1 $m \cdot s^{-1}$) and under vertical wind (4 $m \cdot s^{-1}$) to examine the role of forced convection. Under horizontal wind, all assemblies improved thermal resistance by ~40%, with no significant differences among opening ratios or positions. Under vertical wind, the nonwoven alone lost more than 80% of its insulation, while above-positioned lattices restored and surpassed baseline performance. The lattice with a 25% opening ratio delivered a notable improvement, increasing thermal resistance by over 350% while generating high airflow resistance. Pressure-drop results showed that lower opening ratios impose higher airflow resistance, directly correlating with insulation gains. Statistical analysis confirmed the strong effects of opening ratio and orientation on thermal performance. The findings demonstrate that lattice geometry provides a tunable structural lever for controlling convective heat loss in porous materials, offering fundamental insight into geometry-dependent thermal transport relevant to advanced insulating systems.

1. Introduction

Working in cold environments poses both immediate and long-term risks to human health and performance. Consequently, thermal protective clothing designed for cold temperatures must possess high thermal resistance (R_{ct}) to minimize heat loss from the body to the environment. ISO 11092 standard [1], also known as the "Sweating Guarded Hotplate" test, described methods for measuring the thermal resistance of textiles under steady-state conditions. The method involves placing a test specimen on a heated metal plate set to human skin temperature (35°C). A controlled environment, at 20°C, 65% relative humidity (RH), and a horizontal airflow of 1 $m \cdot s^{-1}$, is maintained above the specimen. The thermal resistance is calculated as the temperature difference between the two surfaces of the material, divided by the heat flux per unit area, expressed in $m^2 \cdot K \cdot W^{-1}$. A more commonly used thermal resistance unit in the textile industry is clo, where 1 clo is equivalent to 0.155 $m^2 \cdot K \cdot W^{-1}$, which is the amount of insulation that allows a person at rest to maintain thermal comfort in a room at 21°C with 50% RH [2].

Although ISO 11092 standard [1] measures thermal resistance under a single, low-speed horizontal airflow, multiple studies have demonstrated that real-world conditions, especially wind, have a profound effect on thermal resistance. Ke et al. showed that wind speed and penetration reduces insulation across different garments, highlighting the role of design elements such as collars and hoods in reducing wind infiltration [3,4]. Shen et al.'s computational fluid dynamics (CFD) analysis revealed that higher wind velocities and air permeability substantially lower thermal resistance by enhancing convective heat transfer in porous textile structures [5]. Zemzem et al. showed that in

* Corresponding author at: Dept. of Mechanical Engineering, École de Technologie Supérieure, 1100 Notre-Dame West, Montréal, Quebec, Canada.
E-mail address: mostafa.alakhdar.1@ens.etsmtl.ca (M. Alakhdar).

https://doi.org/10.1016/j.pes.2026.100285
Received 10 February 2026; Received in revised form 25 March 2026; Accepted 14 April 2026
Available online 15 April 2026

extreme-cold conditions, variations in temperature, humidity, and wind affected insulation performance, offering guidance for optimizing protective gear [6]. Alakhdar et al. reported that wind speed and orientation affect the thermal resistance of nonwoven textiles, with increased vertical wind having a more pronounced effect in reducing thermal resistance [7].

Thermal protection provided by clothing is reduced by increased body motion, wind ↱speed, and moisture; the magnitude of the reduction depends on the fabric's ↱permeability [8–10]. Optimizing cold-weather protective clothing requires improving thermal properties of its constituent materials while maintaining physical comfort and mobility [11]. Recent advancements in thermal protective clothing have explored innovative structures. Dai et al. introduced a hollow three-layer structure, with cavities and pillars, that outperforms other structures in thermal protective performance and air permeability [12]. Du and Li integrated lightweight, breathable honeycomb structures into the thermal liner of multilayer fabric systems, for firefighters' protective clothing, and demonstrated that they significantly enhanced thermal protection compared to traditional fabric designs [13]. Building on this, Dai and Li compared the influence of various hole shapes in honeycomb structures, in the thermal barrier layer, on thermal protection performance and moisture resistance. They identified the best geometry that minimized radiant heat transfer while allowing moisture evaporation [14]. Tu et al. showed that increased wind speed and fabric permeability sharply reduce thermal resistance [15]. These studies, while innovative, tested structures under single-condition environments that did not account for varying factors that occur in real-world settings, such as windy conditions.

Emerging technologies offer new avenues for innovation. 3D printing has gained significant attention for its ability to precisely engineer textile structures, integrating functional materials and complex geometries that can be tailored to enhance thermal performance. Jin et al. showed that 3D-printed carbon fiber-reinforced polylactic acid (PLA) monofilaments improved thermal conductivity and tensile strength, though monofilaments aren't representative of full-scale textile systems [16]. Fajardo et al. examined the mechanical and comfort properties of 3D-printed structures, which offered valuable insights into tensile behavior and wearability, but did not assess thermal performance [17]. Yang et al. embedded 3D-printed nonwoven lattices with phase-change materials (PCMs) which successfully moderated temperature, though concerns remain regarding their durability and performance [18]. Dhangar et al.'s comprehensive review of sustainable 3D-printed materials with thermal insulating properties lacked experimental and practical case studies in textile applications [19]. Liu et al. used additive manufacturing to create 3D-printed breathable, flexible lattice textiles that improved air permeability, moisture management, and thermal comfort, though their performance under variable environmental conditions was not fully explored [20]. Li's review of fused deposition modeling (FDM) in textiles highlighted design flexibility and rapid prototyping but noted that limited material options and functional evaluations are barriers to further development [21].

While previous studies have explored the thermal behavior of materials and some 3D-printed structures, the combined impact of 3D-printed cubic lattice geometry, wind speed and direction, and air permeability on the thermal resistance of bio-based textile assemblies has yet to be conducted. This study investigates the thermal resistance of a composite assembly made from a technical bio-based nonwoven and a 3D-printed cubic lattice with five opening ratios (0, 25, 50, 75, and 100%), tested in two arrangements; one with the lattice positioned adjacent to the skin model (DOWN), and the other with the lattice facing the external environment (UP). Thermal resistances were evaluated under standard ISO 11092 conditions (20°C, 65% RH, and 1 $m{\cdot}s^{-1}$ horizontal airflow), and under a vertical wind speed of 4 $m{\cdot}s^{-1}$. Measurements were conducted using a guarded hotplate system, coupled with a controlled wind source. The pressure-drop across the cubic lattice was also assessed and a statistical analysis of thermal resistance was performed.

2. Materials and methods

This section describes the materials used to prepare the textile–lattice assemblies and the experimental methods employed to evaluate their aerodynamic and thermal performance. The materials subsection details the characteristics of the bio-based nonwoven and the cubic lattice structures, while the methods subsection outlines the pressure-drop measurements, thermal resistance testing, uncertainty analysis, and statistical procedures.

2.1. Materials

2.1.1. Nonwoven textile

In this study, a technical bio-based textile assembly (BTA) was chosen as the textile structure for our experimental investigation. This textile structure is commercially available and has already been characterized [7,22]. The BTA is a nonwoven structure with a single layer of milkweed, kapok, and polylactic acid (PLA) fibers. These are sandwiched between two films of solid PLA fibers, which maintain the structural integrity of the fiber matrix, and are then covered with a layer of nylon protective film on each side.

The physical properties of the BTA assembly are shown in Table 1, where mass per unit area was determined using ISO 9073–1 [23], while thickness and air permeability were determined according to ISO 9073–2 [24] and ASTM D737–18R23 [25], respectively.

2.1.2. Cubic lattice structure

The cubic lattice (CL) was modeled in SolidWorks® 3D CAD software, with each unit cell measuring 9 × 9 × 10 mm. These cells were tiled in both horizontal and vertical directions to create specimens of varying size for different tests. Wall thickness was fixed at 1 mm to preserve the lattice's flexibility and low weight. Geometric details of the cubic lattice are presented in Fig. 1.

Five distinct cubic lattices were each characterized by a unique opening ratio (0, 25, 50, 75, and 100%) calculated using Eq. 1. The opening ratio is defined based on the projected top surface of the ↱lattice. An opening ratio of 100% denotes a completely open lattice and an opening ratio of 0% denotes a completely closed lattice, regardless of the presence of the side walls of the unit cells. Thus, the total area (A_{total}) corresponds to the sum of the projected areas of the square ↱openings within the top unit cells when they are all open; the open area (A_{open}) corresponds to A_{total} minus the sum of the projected closed areas.

$$Opening\ Ratio\ \ (\%) = \frac{A_{open}}{A_{total}} \times 100 \tag{1}$$

The cubic lattices were printed via fused deposition modeling (FDM) on a Qidi Tech I-Fast™ 3D printer. Printing parameters are detailed in Table 2.

All lattices were produced using a flexible PLA filament from ATARAXIA ART®. As a bio-based thermoplastic derived from renewable resources like corn starch and sugarcane, PLA serves as a sustainable alternative to petroleum-derived plastics, offering a lower carbon footprint during production [26]. Its widespread availability and low melting point make it the primary material for FDM printers, providing an accessible and cost-effective way for reproducible rapid prototyping

Table 1
Specifications of BTA assembly.

Specification	Value
Mass per unit area ($g{\cdot}m^{-2}$)	271.6 ± 5.0
Thickness at 0.5 kPa ($\cdot 10^{3}$ m)	5.6 ± 0.5
Air permeability ($cm^{3}{\cdot}s^{-1}{\cdot}cm^{-2}$)	6.9 ± 0.5
Porosity (%)	98.2

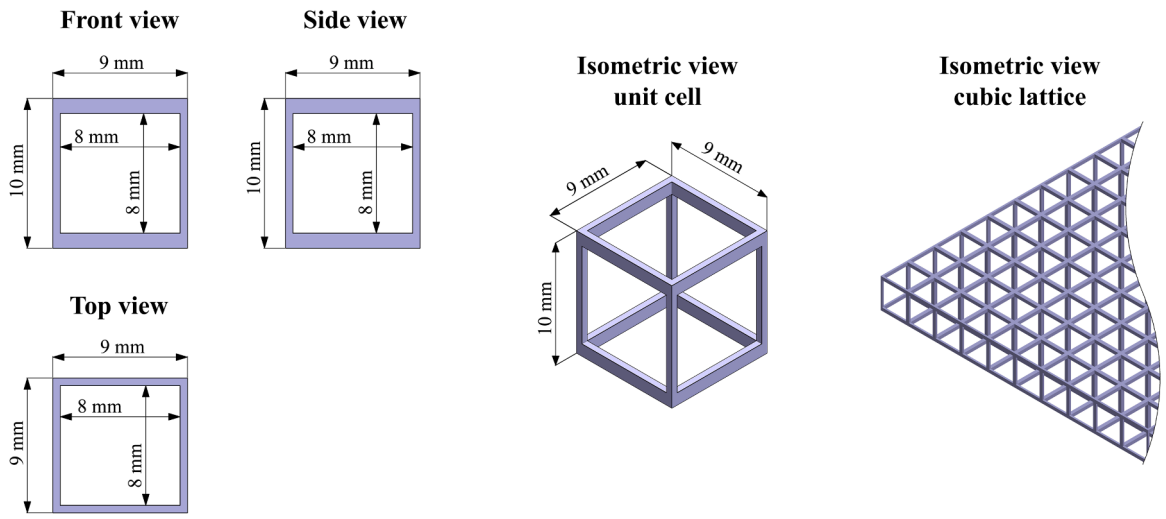

Fig. 1. Cubic lattice structure and dimensions.

Table 2
Cubic lattice printing parameters.

Parameter	Value
Filament diameter	1.75 mm
Nozzle diameter	0.6 mm
Printing temperature	210°C
Printing speed	50 mm·s^{-1}
Bed temperature	40°C
Layer height (excluding first layer)	0.3 mm

[27]. Furthermore, PLA possesses a low intrinsic thermal conductivity (0.13 −0.17 W·m^{-1}·K^{-1}) which, when paired with FDM's ability to create porous cellular architectures, qualifies it as an excellent candidate for thermal insulation [28]. In terms of end-of-life management, PLA is industrially compostable and recyclable, which can significantly reduce environmental toxicity and non-renewable energy demand compared to traditional thermoplastics [29,30]. The mechanical properties of the used filament are presented in Table 3.

Fig. 2 illustrates the five lattice geometries corresponding to the selected opening ratios. To avoid geometric bias in airflow and heat transfer, the arrangement of closed and open areas on the lattice's top surface was randomized using the online random number generator *Randomizer* (https://www.randomizer.org). Each square cell on the lattice's top layer was first assigned a unique identification number in the CAD layout. For each target opening ratio, a specific fraction of these cells was randomly selected and designated as closed surfaces, while the rest remained open. For instance, in the 75% opening ratio configuration, one quarter of the total grid cells were randomly chosen to be closed, representing 25% of the total surface area.

The randomization process was repeated independently for each target opening ratio to ensure statistical independence and avoid pattern regularity that could influence the experiments. Additionally, three random distributions of closed and open cells were generated for each opening ratio, and all three were tested separately under all experimental conditions. The variability associated with this randomization is reflected in the reported standard deviations and is included in the overall experimental uncertainty.

Table 3
Flexible PLA properties [31].

Property	Value
Density	1.24 g·cm^{-3}
Tensile strength	6 −10 MPa
Bending strength	207 MPa
Elongation at break	580 −600%
Melting point	138°C
Shore hardness	89 A

Only the top layer of the lattice was modified to maintain a low surface density, as shown in Fig. 2. To ensure a consistent weight per unit area among all lattices, except for the fully open CL100, the top-layer thickness was adjusted to 0.1 mm, 0.13 mm, 0.2 mm, and 0.4 mm for CL00, CL25, CL50, and CL75 respectively. As textile assemblies must exhibit non-zero air permeability, the fully closed (0% opening ratio) lattice, being impermeable, was included as a reference for comparison.

2.1.3. Assembly

To assess the influence of wind on the final assembly, composed of the nonwoven BTA and the CL with varying opening ratios, two assembly configurations were selected: the "UP" arrangement shown in Fig. 3A (nylon protective film, cubic lattice, nonwoven, nylon protective film), and the "DOWN" arrangement shown in Fig. 3B (nylon protective film, nonwoven, cubic lattice, nylon protective film). In both arrangements, the top surface of the lattice, i.e., the side where the cells are partially open or closed, is oriented upward, facing away from the skin model.

To ensure structural integrity during testing, all layers of the assembly (nonwoven, lattice, and nylon films) were first sewn together along their perimeter. The specimen was then secured to the skin model using an impermeable adhesive tape applied exclusively along the outer guard zone. The measuring zone remained completely free of tape or external constraint, ensuring that no artificial compression or edge effects influenced the thermal resistance measurements.

2.2. Methods

2.2.1. Pressure-drop measurements

The pressure-drop (ΔP) across the cubic lattices alone, under a constant air velocity of 4 m·s^{-1}, was measured using the apparatus presented in Fig. 4. The cubic lattices were placed in the wind tunnel at a distance equal to 10 times the diameter of the pipe to ensure the velocity profile stays the same across the section of the pipe before entering the structures. Upstream and downstream static pressures were recorded, and their difference was used to calculate ΔP, as in Eq. 2.

$$\Delta P = P_u - P_d \tag{2}$$

Where ΔP is the pressure-drop in the cubic lattice, in Pa. P_u and P_d are

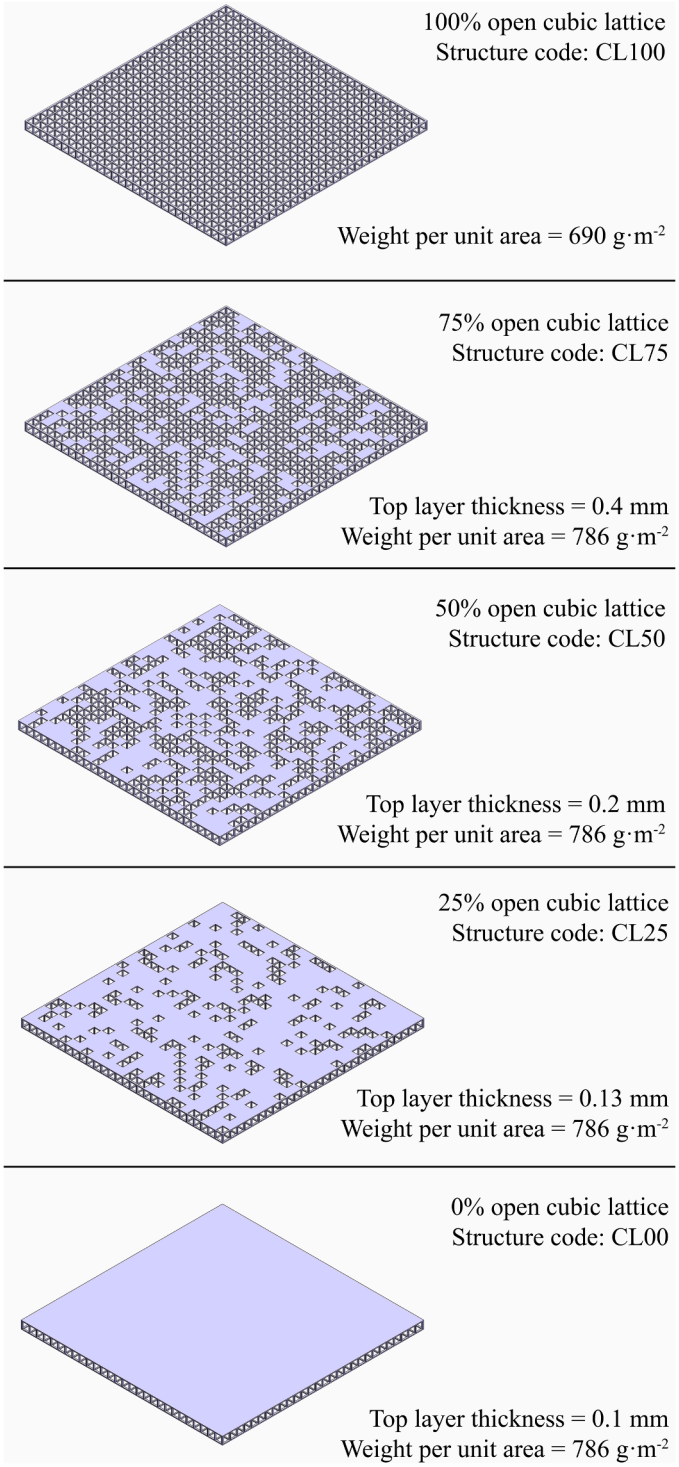

Fig. 2. Cubic lattices with different opening percentages.

the upstream and downstream static pressures, respectively, in Pa.

2.2.2. Thermal resistance testing

The thermal resistance of the entire composite assembly, including the nonwoven textile and the integrated cubic lattice structure, was determined using a skin model apparatus, in two configurations presented in Fig. 5, designed and validated in accordance with the bench-test protocol of ISO 11092 standard [1]. The skin model consists of two plates; the top plate contains the measuring zone (203 × 203 mm) surrounded by a ring-shaped guard zone, while the bottom plate serves as a guard zone beneath the measuring area. The total plate area was 0.09 m^2 (305 × 305 mm); the tested samples measured 305 × 305 mm in order to cover the plate and guard ring. The skin model was maintained at 35°C ± 0.2°C in a controlled environment at 20°C and 65% RH.

Each specimen was preconditioned for at least 24 h at 20°C and 65% RH, as specified by ISO 11092 standard [1]. Thermal resistance of each test specimen was measured under two wind conditions: 1 $m{\cdot}s^{-1}$ horizontal wind and 4 $m{\cdot}s^{-1}$ vertical wind. The selection of these wind conditions was guided by both standard testing protocols and prior experimental evidence. The horizontal wind velocity of 1 $m{\cdot}s^{-1}$ corresponds to the reference condition defined by the ISO 11092 standard [1], ensuring comparability with conventional thermal resistance measurements. In contrast, the vertical wind condition at 4 $m{\cdot}s^{-1}$ was chosen to represent a more severe convective environment, where airflow directly impinges on the textile surface and promotes air penetration within the fibrous structure [6,7,32]. Alakhdar et al. have shown that increasing wind speed from 1 to 4 $m{\cdot}s^{-1}$ leads to a reduction in thermal resistance of the textile of approximately 50% under horizontal wind, compared to about 80% under vertical wind [7]. These results demonstrate that vertical airflow induces significantly greater degradation due to enhanced convective heat transfer and internal air movement. Consequently, the present study contrasts a standardized baseline condition with a high convection scenario, enabling the evaluation of thermal resistance of the proposed structures under these conditions.

Once a thermal steady state of (35 ± 0.2°C) was attained, data was recorded every second for at least 20 min and then averaged to calculate the thermal resistance using Eq. 3. Each assembly was tested in three independent trials (three replicates) under identical testing conditions.

$$R_{ct} = \frac{A \times (T_m - T_a)}{H} - R_{ct0} \tag{3}$$

Where:

R_{ct} is the thermal resistance of the tested sample, in $m^{2}{\cdot}^{\circ}C{\cdot}W^{-1}$;

A is the area of the tested sample, in m^2;

T_m the temperature of the measuring zone of the plate, in °C;

T_a is the temperature of the air, in °C;

H is the heating power supplied to the measuring zone, in W; calculated using Eq 4.

$$H = RI^2 \tag{4}$$

where R is the electrical resistance of the heating element (Ω), measured once and assumed constant during all tests, and I is the measured electrical current supplied to the heater (A).

R_{ct0} is the thermal resistance of the boundary layer above the tested sample, in $m^{2}{\cdot}^{\circ}C{\cdot}W^{-1}$; As this parameter depends on wind speed and direction, it was determined separately for each test condition using Eq. 5 where H_0 is the heating power required to maintain the measuring unit at T_m in its bare state (W).

$$R_{ct0} = \frac{A \times (T_m - T_a)}{H_0} \tag{5}$$

2.2.3. Uncertainty analysis

The uncertainties associated with the experimental measurements were evaluated following the method of propagation of error [33]. Two sources of uncertainty were considered: the random variability observed in repeated measurements (standard deviation), and the systematic uncertainties associated with the instruments used to measure temperature, electrical current, electrical resistance, airflow velocity, and pressure-drop.

For each derived parameter (U), the propagated measurement uncertainty (δU) was calculated using Eq. 6.

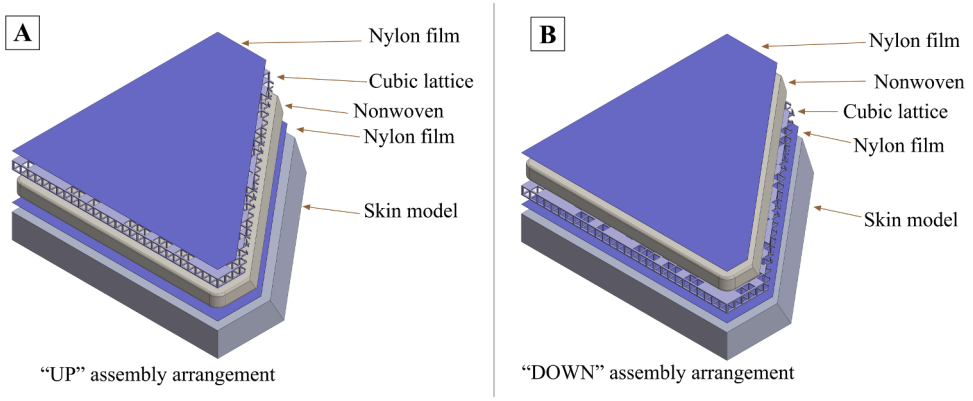

Fig. 3. UP (A) and DOWN (B) assembly arrangements.

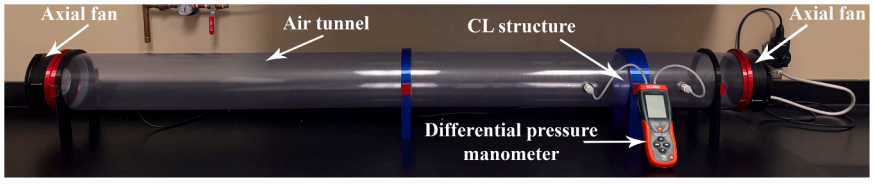

Fig. 4. Pressure-drop measuring apparatus.

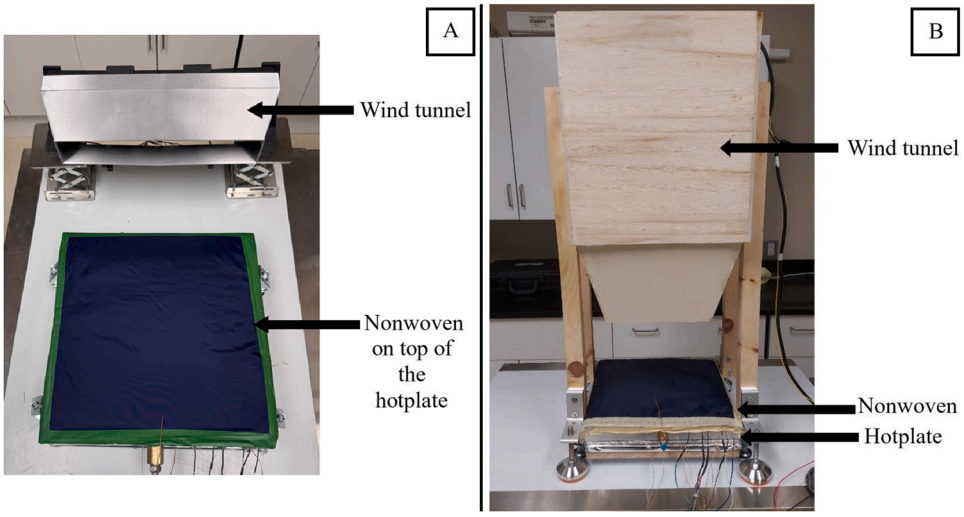

Fig. 5. Testing setup with the horizontal wind tunnel (A), and vertical wind tunnel (B). Reproduced from [7] under the terms of Creative Commons Attribution 4.0 License.

$$(\delta U)^2 = \sum_{i=1}^{n} \left(\frac{\partial U}{\partial x_i}\right)^2 (\delta x_i)^2 \tag{6}$$

where x_i represents each independent measured variable and δx_i its corresponding instrumental uncertainty.

To quantify the random error, each configuration was tested three times, and the standard deviation (σ_U) of the repeated measurements was used as the estimate of repeatability and was calculated using Eq. 7.

$$\sigma_U = \left(\frac{1}{2}\sum_{j=1}^{3} (U_j - \overline{U})^2\right)^{\frac{1}{2}} \tag{7}$$

Because the propagated measurement uncertainty and the repeatability error are statistically independent, they were combined using the Root Sum Squared method to obtain the total uncertainty (δU_{total}) associated with each reported value using Eq. 8:

$$\delta U_{\text{total}} = \sqrt{(\delta U)^2 + \sigma_U^2} \tag{8}$$

These total uncertainties were used as the error bars in all graphical results, ensuring that both instrument accuracy and experimental repeatability are consistently represented.

The measurement uncertainties associated with each instrument used in this study are summarized in Table 4. These values reflect the manufacturer specified accuracy of the instruments and were used as input parameters in the propagation of error analysis.

2.2.4. *Statistical analysis of thermal resistance*

To determine whether the differences in mean thermal resistance among the five cubic lattices of different opening ratios were statistically significant, a one-way analysis of variance (ANOVA) was conducted

Table 4
Measurement instruments, the parameters they recorded, and their associated uncertainties.

Instrument / Sensor	Measured parameters	Uncertainty
Thermocouple	T_m , T_a	1.1°C
Differential pressure manometer	ΔP	3 Pa
Hall effect current transducer	I	1%
Digital multimeter	R	0.9%
Hot wire anemometer	Wind velocity	3%
Hygrometer	Relative humidity	3%

using Minitab® statistical software (version 22, Minitab LLC, USA). This analysis assessed whether the mean thermal resistance values differed significantly across the groups. The null hypothesis (H_0) assumed that all groups have equal mean thermal resistance values, while the alternative hypothesis (H_1) stated that at least one group differs significantly from the others. Following the ANOVA, Tukey's Honestly Significant Difference (HSD) post-hoc test was applied to identify specific pairwise differences between the opening ratio levels. This approach allowed for a detailed comparison of the groups and confirmed which differences were statistically significant at the 95% confidence level ($p < 0.05$).

3. Results and discussion

3.1. Pressure-drop across CL structures

Fig. 6 presents ΔP measured across the cubic lattice structures with varying opening ratios (CL100, CL75, CL50, and CL25) under a vertical airflow of 4 m·s^{-1}. The data reveals a clear inverse relationship between the opening ratio of the CL and the measured ΔP, confirming that as the opening ratio decreases, airflow resistance increases.

The CL100 configuration, characterized by maximum 100% opening percentage, exhibited the lowest ΔP at 9.6 Pa, reflecting minimal obstruction to airflow. As the opening ratio decreased to 75% (CL75), ΔP increased to 20.3 Pa, indicating a moderate rise in airflow resistance due to partial obstruction of the surface. The ΔP across the CL50 structure, with half of its surface area open, rose to 36.4 Pa. The CL25 structure demonstrated the highest ΔP, reaching 70.1 Pa, which represents an approximate seven-fold increase compared to the CL100 structure. This substantial resistance to airflow in the CL25 configuration reflects its enhanced capacity to impede air penetration.

3.2. Thermal resistance

3.2.1. Effect of lattice position and opening ratio at 1 m·s^{-1} horizontal airflow

The thermal resistance of the base nonwoven structure (BTA) alone was 2.51 clo under horizontal wind of 1 m·s^{-1}, as shown in Fig. 7. When combined with the CL, an increase in thermal resistance (averaging at 3.52 clo or 40%) was observed across all configurations, regardless of the CL opening ratio or position.

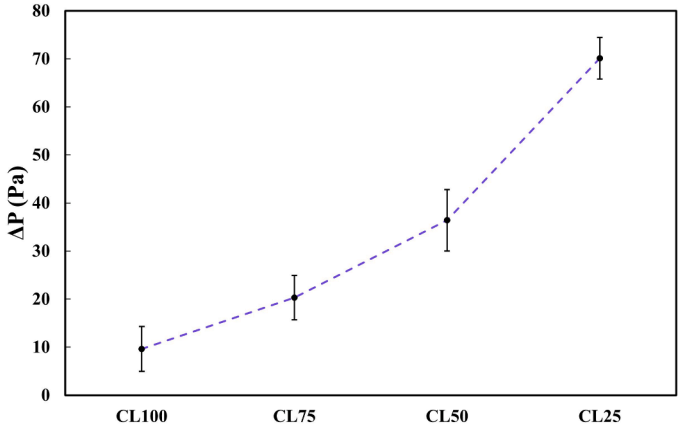

Fig. 6. Pressure-drop across the cubic lattices under air speed of 4 m·s^{-1}.

The thermal resistance of BTA+CL100 in the DOWN arrangement increased by approximately 41% compared to the BTA alone. Similarly, in the UP position, the resistance was still elevated, with an increase of approximately 32%, but slightly lower than the DOWN arrangement. This pattern suggests that under horizontal wind of 1 m·s^{-1}, placing the CL beneath the BTA provides a slightly better insulation effect, likely due to reduction of convective losses from the bottom and enhancement of air trapping within the BTA structure. As the opening percentage of the CL decreased, the overall thermal resistance values remained high and quite consistent. This indicates that once the CL structure disrupts the airflow, further reductions in the opening ratio does not significantly improve thermal resistance under this low-speed airflow condition.

3.2.2. Effect of lattice position and opening ratio at 4 m·s^{-1} vertical airflow

In contrast, Fig. 8 shows the behavior of the same assemblies under vertical airflow at 4 m·s^{-1}, simulating forced convection as experienced in windy environments. Here, the thermal resistance of BTA alone dropped sharply to 0.46 clo, representing over 80% reduction compared to its performance under horizontal airflow of 1 m·s^{-1}. This substantial decrease is due to forced vertical airflow enhancing convective heat transfer, pushing air through the porous material and disrupting insulating air layers within the structure [7].

Although the integration of the cubic lattice increases the total thickness of the assembly, thickness alone cannot account for the observed differences in thermal resistance. Assemblies with the same thickness but different lattice opening ratios exhibited substantially different thermal resistances under vertical wind, indicating that airflow resistance and convective heat transfer suppression govern the thermal response.

The ΔP measurements provided critical preliminary insight into the airflow resistance characteristics of the CL structures, which directly influenced the thermal performance of the assemblies under forced convection conditions. As expected, a clear inverse relationship was observed between lattice opening ratio and ΔP values, confirming that lower opening ratios significantly impede airflow penetration. The fully closed lattice (CL00) functioned as an effective wind barrier, while the highly permeable CL100 structure generated the lowest ΔP (9.6 Pa), reflecting minimal resistance to airflow.

This aerodynamic behavior was strongly reflected in the thermal resistance results under identical wind exposure. The BTA+CL00 (UP) configuration achieved a thermal resistance of approximately 3.3 clo, corresponding to an increase of over 600% compared to the BTA alone. The CL00 layer, acting as a continuous, non-porous surface, prevented direct airflow infiltration, forcing the incident wind to divert laterally. This lateral deflection created zones of stagnant air above the BTA, preventing air movement in the assembly.

The BTA+CL25 (UP) assembly achieved a thermal resistance of approximately 2.2 clo, an improvement of over 350% compared to BTA alone. The corresponding ΔP of 70.1 Pa indicates substantial airflow resistance despite the partial lattice openings. In this configuration, the limited wind penetration is insufficient to disrupt the insulating air pockets. Furthermore, the interaction of the airflow with the lattice geometry induces velocity reduction, diminishing the convective transport of thermal energy toward the BTA layer.

For assemblies incorporating CL50, CL75, and CL100 in the UP configuration, a progressive reduction in thermal resistance was observed, consistent with increasing opening ratio and decreasing ΔP values. As the lattice opening ratio increased, the structure's capacity to obstruct or redirect vertical airflow diminished. In particular, the CL100 configuration still demonstrated a modest improvement in thermal resistance relative to BTA alone. This improvement can be attributed to geometric flow disruption within the lattice, which, even without

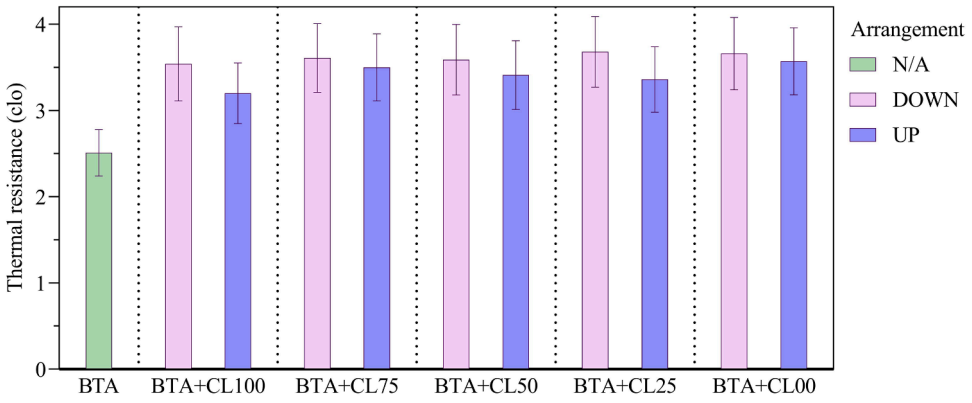

Fig. 7. Thermal resistance of BTA+CL structures under horizontal wind of 1 $m \cdot s^{-1}$.

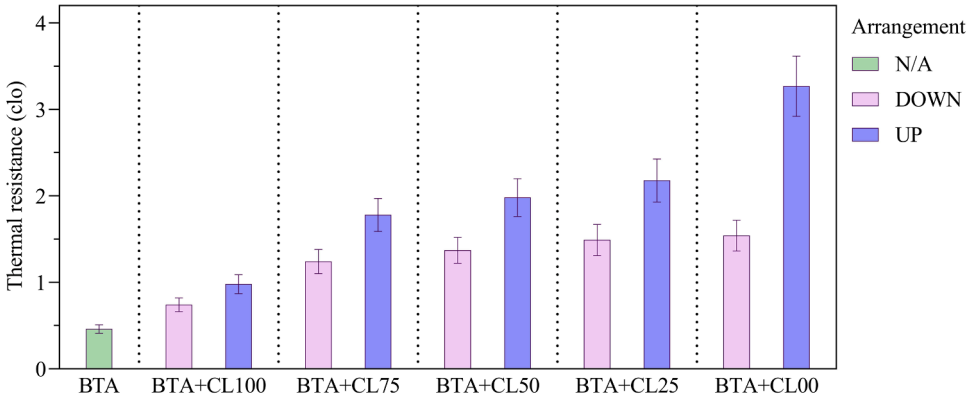

Fig. 8. Thermal resistance of BTA+CL structures under vertical wind of 4 $m \cdot s^{-1}$.

significant blockage, introduces turbulence and partially deflects the incident airflow, reducing the net heat transfer.

In the DOWN configuration, where the CL layer is positioned beneath the BTA, thermal resistance values were markedly lower, ranging from approximately 0.7 –1.5 clo across the different assemblies. In this arrangement, the vertical airflow directly impacts the exposed BTA nonwoven layer, which, due to its high porosity (~98%), permits significant airflow infiltration. The CL layer offers limited mitigation of convective effects, regardless of its opening ratio. Even in configurations with lower lattice opening ratios, where the CL exhibits higher airflow resistance, its downstream position relative to the wind renders less effective as a primary barrier.

These findings emphasize the critical importance of CL placement. In the UP configuration, the CL intercepts and disrupts the incident airflow before it reaches the porous BTA layer, significantly reducing convective heat loss. In contrast, the DOWN configuration allows airflow to penetrate the insulation layer before encountering any structural resistance, leading to displaced internal air and accelerated heat transfer.

While the simple cubic lattice geometry was utilized in this study to establish a fundamental baseline for wind-induced heat loss, alternative topologies such as Gyroid or Diamond Triply Periodic Minimal Surfaces (TPMS) may offer further optimization. Literature suggests that while cubic lattices provide clear orthogonal pathways for airflow, more tortuous TPMS geometries could potentially enhance thermal resistance by further suppressing internal convection and increasing the path length for heat transfer [20,34].

3.3. Statistical analysis of the thermal resistance

A one-way analysis of variance (ANOVA) was conducted to investigate the effect of lattice opening ratio on the thermal resistance of assemblies exposed to both horizontal and vertical wind, considering two lattice positions relative to the nonwoven layer (UP and DOWN). The assumptions of normality and homogeneity of variance were verified using the Kolmogorov–Smirnov and Levene's tests, respectively, with all p-values exceeding 0.05, confirming that the datasets met ANOVA requirements.

Under horizontal wind exposure at 1 $m \cdot s^{-1}$ with the lattice positioned beneath the nonwoven, the ANOVA model yielded $p < 0.05$ and an R^2 of 94.1%, indicating that all lattice assemblies significantly improved thermal resistance compared to the nonwoven alone (BTA). The corresponding Tukey post-hoc comparisons are presented in Fig. 9A. Although all lattice configurations enhanced thermal resistance relative to BTA, differences among assemblies with varying opening ratios were not statistically significant, as confidence intervals overlapped and crossed zero. Similar results were obtained when the lattice was positioned above the nonwoven layer under horizontal wind, where ANOVA indicated $p < 0.05$ with an R^2 of 94.7%. Again, all lattice assemblies provided increased thermal resistance relative to BTA, yet no significant differences were observed between the different lattice designs (Fig. 9B).

In contrast, under vertical wind exposure at 4 $m \cdot s^{-1}$ with the lattice positioned beneath the nonwoven layer, ANOVA results showed $p < 0.05$ with an R^2 of 98.7%, confirming significant improvements in thermal resistance for all lattice assemblies compared to BTA. As shown in Fig. 9C, Tukey's post-hoc analysis revealed significant statistical differences between specific configurations. The assembly incorporating the fully closed lattice (BTA+CL00) provided the highest thermal resistance, significantly outperforming the assembly with the fully open lattice (BTA+CL100) and intermediate assemblies. However, overlapping confidence intervals between certain adjacent configurations (e.g., BTA+CL25 vs. BTA+CL00 and BTA+CL50 vs. BTA+CL25) suggest minimal performance differentiation at specific opening ratios.

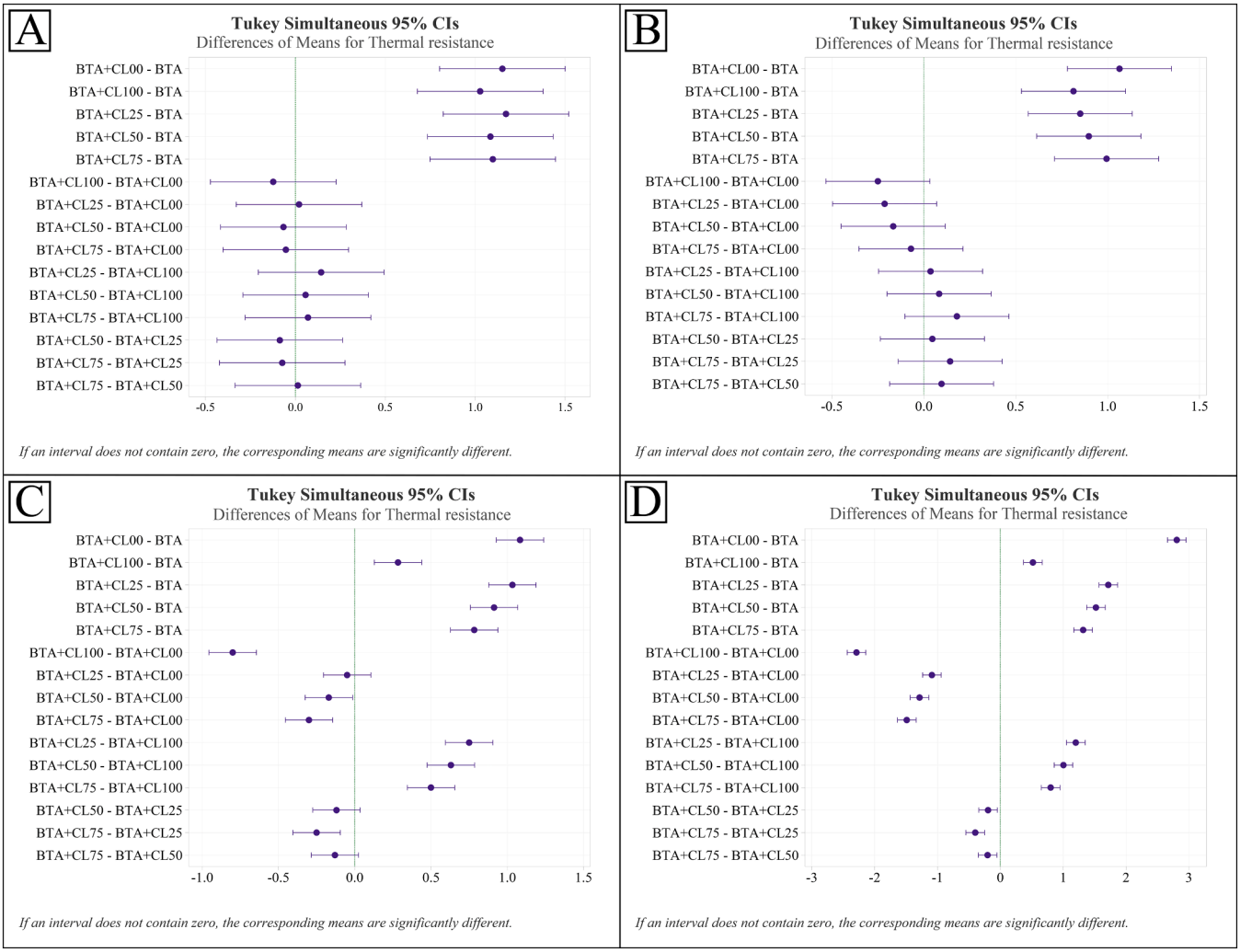

Fig. 9. Tukey post-hoc analysis of thermal resistance across lattice assemblies.

Furthermore, under vertical wind with the lattice positioned above the nonwoven, ANOVA results demonstrated $p < 0.05$ and an R^2 of 99.8%, with Tukey's comparisons indicating significant differences across all lattice configurations as shown in Fig. 9D. In this case, the fully closed lattice (BTA+CL00) again exhibited the highest thermal resistance, significantly exceeding that of all other assemblies.

Overall, these results confirm that lattice structures consistently improve thermal resistance across all tested conditions. However, the influence of lattice opening ratio and positioning becomes increasingly pronounced under vertical wind exposure, particularly when the lattice is placed above the nonwoven layer.

4. Conclusion

This study demonstrates that integrating 3D-printed cubic lattice structures into a bio-based nonwoven assembly can significantly mitigate wind-induced thermal losses by controlling convective heat transfer. Under standard horizontal airflow conditions (1 $m{\cdot}s^{-1}$), all lattice-integrated assemblies exhibited an average increase of approximately 40% in thermal resistance compared to the nonwoven alone, with limited sensitivity to lattice opening ratio or placement. In contrast, under vertical wind exposure (4 $m{\cdot}s^{-1}$), the nonwoven experienced a severe degradation of thermal resistance, whereas lattice-integrated configurations, particularly when the lattice was positioned above the nonwoven, effectively restored and enhanced thermal resistance.

The results highlight the dominant role of airflow interception and redirection in governing thermal performance under forced convection. Pressure-drop measurements confirmed a strong inverse relationship between lattice opening ratio and airflow permeability, directly correlating with the observed thermal resistance trends. While fully closed lattices provided the highest thermal resistance by preventing airflow penetration, partially open lattices achieved substantial thermal improvements by suppressing convective heat transfer while maintaining permeability. Even the fully open lattice demonstrated measurable insulation gains, indicating that three-dimensional lattice geometry alters airflow patterns through flow disruption and redirection, rather than acting solely as a passive barrier.

Unlike traditional windproof layers based on dense, continuous membranes, the lattice-integrated system provides a geometry-driven approach to airflow control. By tuning lattice opening ratio and placement, convective heat loss can be mitigated without fully eliminating permeability, offering a flexible pathway for balancing thermal resistance and pressure-drop in textile assemblies.

From a design perspective, although the fully closed lattice yielded the highest thermal resistance, its impermeable nature limits applicability in clothing systems requiring moisture transport. Considering both thermal and aerodynamic performance, the 25% open lattice positioned above the nonwoven emerges as a favorable compromise, delivering substantial thermal resistance enhancement while preserving airflow pathways. Overall, the findings establish cubic lattice geometry as an effective structural lever for managing wind-induced heat loss and provide a foundation for the development of advanced, multifunctional

insulating systems for cold-weather protective applications.

From an economic perspective, additive manufacturing techniques such as fused deposition modeling offer high design flexibility and enable the fabrication of complex, tunable structures that are not achievable with conventional textile processes. However, these advantages are currently associated with longer production times and higher costs, which may limit large-scale implementation. Ongoing advances in additive manufacturing technologies are expected to improve scalability and cost-efficiency, further supporting the potential integration of such structures into future textile systems where tailored thermal behavior is required.

5. Limitations

This study's limitations indicate several avenues for future research. To gain a more accurate understanding of the cubic lattice and hollow structures' performance, more testing environments that replicate realistic conditions like high humidity, temperature variations, and mechanical stress are essential. Furthermore, the long-term effects of wear and washing, as well as their interaction with other garment layers, require investigation. Additionally, the assessment of evaporative resistance and moisture vapor transmission remains an area for future consideration, as these properties are important for a comprehensive view of physiological comfort. Future work could also explore alternative geometric patterns beyond the cubic structures and optimize multilayer fabric systems tailored for specific applications.

CRediT authorship contribution statement

Mostafa Alakhdar: Writing – original draft, Visualization, Software, Methodology, Investigation, Formal analysis, Data curation, Conceptualization. **Ludwig Vinches:** Writing – review & editing, Validation, Supervision, Resources, Project administration, Methodology, Investigation, Funding acquisition, Formal analysis, Conceptualization. **Hallé Stéphane:** Writing – review & editing, Visualization, Validation, Resources, Project administration, Methodology, Investigation, Funding acquisition, Formal analysis, Conceptualization.

Funding

This work was supported by a financial support of our industrial partners, Logistik Unicorp Inc and Eko-Terre Inc, as well as a grant from PRIMA Québec (N° R23–13–001) and the Natural Sciences and Engineering Research Council of Canada (ALLRP 566738–21).

Declaration of Competing Interest

The authors declare that they have no known competing financial interests or personal relationships that could have appeared to influence the work reported in this paper.

Acknowledgments

The authors would like to express their gratitude to the industrial partners in Logistik Unicorp Inc and Eko-Terre Inc.

Data availability

Data will be made available on request.

References

[1] International Organization for Standardization, Textiles — Physiological effects — Measurement of thermal and water-vapour resistance under steady-state conditions (sweating guarded-hotplate test) (Standard No. ISO 11092:2014), (2014).
[2] Kent Michael. The Oxford Dictionary of Sports Science & Medicine, 3rd ed., Oxford University Press, 2006 https://doi.org/10.1093/acref/9780198568506.001.0001.
[3] Y. Ke, G. Havenith, J. Li, X. Li, A new experimental study of influence of fabric permeability, clothing sizes, openings and wind on regional ventilation rates, Fibers Polym. 14 (2013) 1906–1911, https://doi.org/10.1007/s12221-013-1906-5.
[4] Y. Ke, G. Havenith, X. Zhang, X. Li, J. Li, Effects of wind and clothing apertures on local clothing ventilation rates and thermal insulation, Text. Res. J. 84 (2014) 941–952, https://doi.org/10.1177/0040517513512399.
[5] H. Shen, Y. Xu, F. Wang, J. Wang, L. Tu, Numerical analysis of heat and flow transfer in porous textiles - Influence of wind velocity and air permeability, Int. J. Therm. Sci. 155 (2020) 106432, https://doi.org/10.1016/j.ijthermalsci.2020.106432.
[6] M. Zemzem, S. Hallé, L. Vinches, Thermal insulation of protective clothing materials in extreme cold conditions, Saf. Health Work 14 (2023) 107–117, https://doi.org/10.1016/j.shaw.2022.11.004.
[7] M. Alakhdar, L. Vinches, S. Hallé, Assessing thermal resistance of a nonwoven textile under wind exposure: challenging ISO 9920 with experimental insights, J. Ind. Text. 55 (2025), https://doi.org/10.1177/15280837251328908.
[8] K. Jussilia, S. Rissanen, A. Aminoff, J. Wahlström, A. Vaktskjold, L. Talykova, J. Remes, S. Mänttäri, H. Rintamäki, Thermal comfort sustained by cold protective clothing in Arctic open-pit mining—a thermal manikin and questionnaire study, Ind. Health 55 (2017) 537–548, https://doi.org/10.2486/indhealth.2017-0154.
[9] Y.S. Chen, J. Fan, W. Zhang, Clothing thermal insulation during sweating, Text. Res. J. 73 (2003) 152–157, https://doi.org/10.1177/004051750307300210.
[10] Y. Lu, F. Wang, X. Wan, G. Song, W. Shi, C. Zhang, Clothing resultant thermal insulation determined on a movable thermal manikin. Part I: effects of wind and body movement on total insulation, Int. J. Biometeorol. 59 (2015) 1475–1486, https://doi.org/10.1007/s00484-015-0958-1.
[11] E. Kamalha, Y. Zeng, J.I. Mwasiagi, S. Kyatuheire, The Comfort Dimension; a Review of Perception in Clothing, J. Sens. Stud. 28 (2013) 423–444, https://doi.org/10.1111/joss.12070.
[12] J. Dai, Y. Zhang, X. Li, A hollow structure of thermal barrier for thermal protective clothing, Fibers Polym. 25 (2024) 713–724, https://doi.org/10.1007/s12221-023-00464-6.
[13] F. Du, X. Li, The approach of honeycomb sandwich structure for thermal protective clothing, J. Ind. Text. 50 (2021) 957–969, https://doi.org/10.1177/1528083719851844.
[14] J. Dai, X. Li, Effect of different hole shape of thermal barrier on the performance for thermal protective clothing, J. Ind. Text. 51 (2022) 2499S–2513S, https://doi.org/10.1177/15280837221102965.
[15] L. Tu, H. Shen, F. Wang, The effective thermal resistance of permeable textile ensemble in windy environment, Int. J. Therm. Sci. 159 (2021) 106644, https://doi.org/10.1016/j.ijthermalsci.2020.106644.
[16] P. Jin, T. Pan, Y. Li, T. Zhong, J. Jiang, C. Pu, C. Ma, Performance and thermal properties of 3D printed CF-reinforced PLA monofilaments, Coatings 14 (2024) 1479, https://doi.org/10.3390/coatings14121479.
[17] J.I. Fajardo, M.V. Farez, C.A. Paltán, Experimental analysis of the relationship between textile structure, tensile strength and comfort in 3d printed structured fabrics, Polym. (Basel) 15 (2022) 152, https://doi.org/10.3390/polym15010152.
[18] Z. Yang, Y. Ma, S. Jia, C. Zhang, P. Li, Y. Zhang, Q. Li, 3D-printed flexible phase-change nonwoven fabrics toward multifunctional clothing, ACS Appl. Mater. Interfaces 14 (2022) 7283–7291, https://doi.org/10.1021/acsami.1c21778.
[19] M. Dhangar, K. Chaturvedi, M. Mili, S.S. Patel, M.A. Khan, H.N. Bhargaw, A. K. Srivastava, S. Verma, Emerging 3D printed thermal insulating materials for sustainable approach: a review and a way forward, Polym. Adv. Technol. 34 (2023) 1425–1434, https://doi.org/10.1002/pat.5989.
[20] J. Liu, L. Hu, K.-W. Lui, S.W. Wong, S. Jiang, Design and characterization of breathable 3D printed textiles with flexible lattice structures, J. Manuf. Process 141 (2025) 48–58, https://doi.org/10.1016/j.jmapro.2025.02.062.
[21] S. Li, Development and application of fused deposition molding 3D printing technology in textile and fashion design, J. Eng. Fiber Fabr. 19 (2024), https://doi.org/10.1177/15589250241266977.
[22] S.M. Mortazavinejad, M. Alakhdar, L. Vinches, S. Hallé, A novel methodology for calculating thermal conductivity of natural hollow fibers with validation in nonwoven fabric structures, Int. Commun. Heat. Mass Transf. 167 (2025), https://doi.org/10.1016/j.icheatmasstransfer.2025.109269.
[23] International Organization for Standardization, Nonwovens — Test methods — Part 1: Determination of mass per unit area (ISO Standard No. 9073–1:2023), (2023).
[24] International Organization for Standardization, Textiles — Test methods for nonwovens — Part 2: Determination of thickness (ISO Standard No. 9073–2:1995), (1995).
[25] ASTM International, Standard Test Method For Air Permeability Of Textile Fabrics (Standard No. D737–18R23), West Conshohocken, PA: ASTM International, 2023 (2018). https://store.astm.org/d0737–18r23.html.
[26] E.R. Rezvani Ghomi, F. Khosravi, A.S. Saedi Ardahaei, Y. Dai, R.E. Neisiany, F. Foroughi, M. Wu, O. Das, S. Ramakrishna, The life cycle assessment for polylactic acid (PLA) to make it a low-carbon material, Polym. (Basel) 13 (2021) 1854, https://doi.org/10.3390/polym13111854.
[27] I. Plamadiala, C. Croitoru, M.A. Pop, I.C. Roata, Enhancing polylactic acid (PLA) performance: a review of additives in fused deposition modelling (FDM) filaments, Polym. (Basel) 17 (2025) 191, https://doi.org/10.3390/polym17020191.
[28] M. Tychanicz-Kwiecień, S. Grosicki, M. Markowicz, Experimental investigation of thermal conductivity of selected 3D-printed materials, Materials 18 (2025) 3950, https://doi.org/10.3390/ma18173950.

[29] A. Fonseca, E. Ramalho, A. Gouveia, F. Figueiredo, J. Nunes, Life cycle assessment of PLA products: a systematic literature review, Sustainability 15 (2023) 12470, https://doi.org/10.3390/su151612470.
[30] A. Costa, T. Encarnação, R. Tavares, T. Todo Bom, A. Mateus, Bioplastics: Innovation for Green Transition, Polym. (Basel) 15 (2023) 517, https://doi.org/10.3390/polym15030517.
[31] Ataraxia Art, Flexible Polylactic acid - 3D Printer Filament, (2026). https://ataraxiaart.com/.
[32] S.M. Mortazavinejad, L. Vinches, S. Hallé, Thermal resistance analysis of cold-protective clothing using numerical modeling: influence of natural-based nonwoven fabric structure and wind flow conditions, Int. Commun. Heat. Mass Transf. 173 (2026), https://doi.org/10.1016/j.icheatmasstransfer.2026.110802.
[33] R.J. Moffat, Describing the uncertainties in experimental results, Exp. Therm. Fluid Sci. 1 (1988) 3–17, https://doi.org/10.1016/0894-1777(88)90043-X.
[34] A. Gupta, S. Babu L, Triply periodic minimal surfaces: an overview of their features, failure mechanisms, and applications, J. Mines Met. Fuels (2023) 211–221, https://doi.org/10.18311/jmmf/2022/31230.